

Characterization and Modeling of Non-Uniform Charge Collection in CVD Diamond Pixel Detectors

T. Lari^{a,b,1}, A. Oh^c, N. Wermes^b, H. Kagan^d, M. Keil^{c,b},
W. Trischuk^e

^a*INFN and Dipartimento di Fisica, Università di Milano, Via Celoria 16, I-20133,
Milano (Italy)*

^b*Physikalisches Institut der Universität Bonn, Nussallee 12, 53115 Bonn,
Germany*

^c*European Laboratory for Particle Physics (CERN), 1211 Geneva 23, Switzerland*

^d*High Energy Physics Group, Department of Physics, Ohio State University, 174
West 18th Avenue, Columbus, OH, USA*

^e*Department of Physics, University of Toronto, 60 St. George Street, Toronto, ON,
Canada*

Abstract

A pixel detector with a CVD diamond sensor has been studied in a 180 GeV/c pion beam. The charge collection properties of the diamond sensor were studied as a function of the track position, which was measured with a silicon microstrip telescope. Non-uniformities were observed on a length scale comparable to the diamond crystallites size. In some regions of the sensor, the charge drift appears to have a component parallel to the sensor surface (i.e., normal to the applied electric field) resulting in systematic residuals between the track position and the hits position as large as 40 μm . A numerical simulation of the charge drift in polycrystalline diamond was developed to compute the signal induced on the electrodes by the electrons and holes released by the passing particles. The simulation takes into account the crystallite structure, non-uniform trapping across the sensor, diffusion and polarization effects. It is in qualitative agreement with the data. Additional lateral electric field components result from the non-uniform trapping of charges in the bulk. These provide a good explanation for the large residuals observed.

Key words: diamond pixel detector, non-uniform charge collection

PACS: 29.40.Wk, 29.40.Gx

¹ Corresponding author. Tel: +39-0250317391; fax: +39-0250317624. *E-mail ad-*

1 Introduction

In the last decade the quality of chemical vapor deposited (CVD) diamond for particle detectors has greatly improved, and the use of this material has become a potentially attractive option for vertex detectors at high luminosity colliders (such as the LHC after the proposed luminosity upgrade [1]) promising to provide the radiation resistance needed for the challenging particle fluxes expected.

Diamond detectors are believed to be more radiation-hard than silicon [2,3,4]. Even after radiation exposures in excess of 10^{15} hadrons/cm² they can be operated at room temperature without significant leakage current. A loss in the charge signal of about 40% was observed with pion/proton radiation of 5×10^{15} p/cm² [2,3]. With neutrons a loss of 30% was observed at a fluence of 2×10^{15} n/cm² [3].

The charge collection distance is the figure of merit for diamond particle detectors. It is defined as dQ/Q_0 where d is the diamond film thickness, and Q/Q_0 is the collection efficiency of the ionization charge. The collection distance has been increased from a few micrometers in the beginning of diamond R&D to about 250 μ m, corresponding to a mean signal of 9000 electrons, today [5].

The charge collection distance depends on the presence of charge carrier traps [6]. Once a deep level trap has captured a charge carrier the trap can be permanently passivated. As a consequence of this process, CVD diamond shows a significant increase in the charge collection distance after being exposed to fluences of the order of 10^6 minimum ionizing particles per mm², a process called pumping or priming. CVD diamond remains for a long period (months) in the primed state if kept in the dark and at room temperature.

CVD diamond usually has a polycrystalline structure with an average crystallite size on the growth side of the order of 1/7 of the thickness [3]. On the substrate side the crystal size is only a few micrometers. The charge collection distance can be different in different crystallites [3,7], leading to a non-uniform response and a broadening of the distribution of the charge signal from the whole substrate.

In this paper we report test-beam measurements and simulations of diamond pixel detectors equipped with a prototype electronics chip of the ATLAS Pixel silicon detector [8,9,10]. In Section 2 the analysis of test-beam data taken with two diamond pixel detectors is presented. The spatial resolution and detection efficiency of the detectors are reported, and the observation of a non uniform response of the detectors across the sensor area is discussed. In Section 4 a

dress Tommaso.Lari@mi.infn.it

numerical simulation of the charge collection processes inside the diamond sensor and of the detector response is presented. It is shown that the non uniform response can be reproduced as a consequence of the polarization fields created by the charge trapped in the crystallite structure.

2 Test beam Set-up and tested devices

2.1 The test beam set-up

Test beam experiments were performed at the CERN SPS accelerator during the years 2000 and 2001 with a pion beam of 180 GeV/ c momentum.

A beam telescope consisting of 4 silicon microstrip modules was used to measure the transverse position of the incident beam particles. In the setup used in the year 2000 [11] each module consisted of a pair of microstrip detectors, each providing one coordinate. In the setup used in 2001 each module consisted of a double-sided microstrip detector. The new telescope used a readout architecture including zero suppression [12], which offered higher trigger rate capability. For both set-ups, the position resolution of tracks projected onto the tested devices was about 6 μm .

2.2 The diamond sensors

Two diamond sensors, identified by UTS-5 and CD91, were tested in the beam [13]. The sensors were grown to a thickness of about 800 μm . The grain size on the growth side is of the order of 100 μm . The sensors were then lapped on the substrate side by about 300 μm and on the growth side by about 50 μm so that the final thickness is 432 μm for UTS-5 and 470 μm for CD91. The lateral dimensions of the sensors were 8 mm \times 8mm.

The electrode on the growth side was segmented in pixels of 50 $\mu\text{m} \times$ 400 μm dimensions. Each pixel was electrically connected via electroplated PbSn solder bumps to a matching readout electronics cell in the front-end chip.

In the following, x is the coordinate along the short (50 μm) dimension of the pixels, y is the coordinate along the long (400 μm) dimension of the pixels, and z is the coordinate perpendicular to the pixel plane.

Before operation at the test beam, data were taken with a ^{241}Am and a ^{90}Sr source, with activities of 74 MBq and 62 kBq respectively. The sources were kept for 12 h at about 5 mm from the diamond sensor. The β source delivered

a fluence of the order of 10^7 mm^{-2} (0.3 Gy dose) to each sensor, which is enough to bring good quality diamond in the primed state [7]. This conclusion is supported by the test beam data, discussed below, since the average signal and the detection efficiency did not show any time dependence during the data taking.

2.3 Front-end electronics

The electronics chips were produced during the development phase of the ATLAS Pixel front-end electronics program [8,9,10]. Their design was similar to that of the final front-end electronics for ATLAS Pixel [14,15]. In each front-end chip, 2880 channels are arranged into 18 columns by 160 rows. The charge-sensitive preamplifiers feature a DC feedback scheme with a tunable current providing control over the shaping-time for a given input charge. A discrimination stage sits behind the preamplifier in each channel which is sensitive to the leading edges and the trailing edges of pulses. Each channel is equipped with its own 3-bit DAC for channel-to-channel threshold adjustments, thus a means of overall dispersion reduction is provided. The chips have a 7-bit charge measurement capability using the time-over-threshold (ToT) of the signal. The ToT is calibrated by injecting a known charge into every channel. A 2880-bit pixel register plus one corresponding latch per channel enable individual pixels to be masked-off independently for calibration-strobing and readout.

The chip is operated at the 40 MHz LHC bunch crossing rate and the times are measured in multiples of the 25 ns clock period. Only pixel signals whose leading edge belongs to the period specified by an external trigger are read out. At the test-beam the trigger was provided by two scintillator detectors and 16 consecutive 25 ns time windows were accepted.

During the operation in the test beam the thresholds of the individual channels were adjusted achieving a threshold dispersion of less than 100 e. A typical threshold setting was 1000 e while the average noise per pixel was about 200 e.

3 Analysis of test beam data

Events were filtered with the requirement of one and only one track reconstructed by the silicon microstrip telescope in each event. Only events with a track reconstruction χ^2 probability greater than 0.02 were kept. Tracks were required to extrapolate into a fiducial area. For CD91 this was the surface covered by the pixel array, excluding the region within 40 μm of the border.

For UTS-5 it was the smaller area with a good bump-bonding yield [13].

Pixel clusters were built clustering together all adjacent pixels, independently of track extrapolations. The cluster charge is defined as the sum of the charges measured by the pixels of the cluster. This can be less than the total collected charge, since it does not include the pixel signals below the electronics threshold. The cluster position is computed as the arithmetic mean of the coordinates of the pixels in the cluster.

The data discussed here have been taken at normal incidence. The sensors were operated with a bias voltage of 450 V (UTS-5) or 470 V (CD91).

At normal incidence, most clusters are composed of one or two pixels. The average cluster size was measured to be 1.260 ± 0.001 pixels for CD91 and 1.484 ± 0.010 for UTS-5.

Charge calibrations were available only for UTS-5, for which the cluster charge (the sum of the charges measured by the pixels of the cluster) was (3000 ± 300) electrons. The detection efficiency was $(67.69 \pm 0.10)\%$ for CD91 and $(76.8 \pm 0.5)\%$ for UTS-5.

Fig. 1 shows the distribution of the x residuals between the track position as determined by the telescope and the pixel cluster position. For comparison, the same distribution is reported for an ATLAS Pixel silicon sensor, with a similar pixel geometry, bump-bonded to a similar electronics chip and tested with the same test-beam setup. The r.m.s. of spatial residual distributions² yields resolutions of $(14.46 \pm 0.05) \mu\text{m}$ for the silicon detector, $(23.35 \pm 0.21) \mu\text{m}$ for UTS-5 and $(25.45 \pm 0.11) \mu\text{m}$ for CD91. The usage of charge interpolation algorithms for the position of multi-pixel clusters improves these values only by a few tenths of a micrometer. The values of mean cluster size, detection efficiency and spatial resolution are summarized in table 1.

The reasons for the poor diamond resolution were investigated by looking at the mean x residuals³ as a function of the track position on the sensor. The sensor was divided in bins of $50 \mu\text{m} \times 50 \mu\text{m}$ size, and for each bin i the mean spatial x residual r_i has been computed. The same analysis was also performed on a ATLAS Pixel silicon detector with similar sensor geometry, electronics and test beam setup. The results are reported in Fig. 2⁴.

² The r.m.s. of each distribution is computed between -0.1 mm and 0.1 mm

³ The silicon microstrip telescope provides comparable resolutions on the x and y coordinates of the track extrapolation. The pixel cluster position, in contrast, is determined with far better precision in the x direction, because of the 8:1 aspect ratio of ATLAS Pixels. For this reason, the y residuals have not been taken into consideration.

⁴ Only a small part of the sensor area is covered, to improve the visibility of the

The silicon sensor (upper plot) shows a more uniform distribution. Bins with large residuals are isolated and scattered across the sensor as one expects from statistical fluctuations. The diamond sensors (middle and lower plot) present regions which have systematically positive or negative residuals as large as $40 \mu\text{m}$. No correlation is observed between these regions and the segmentation in pixels. The scale of the residual clustering is of the order of $100 \mu\text{m}$ which is also the typical size of the diamond crystallites. This suggests that in some crystallites the drift of the charge carriers has a component parallel to the sensor surface, so that the average position of the pixel clusters is shifted away from the track position.

The statistical error δr_i on each mean residual r_i is $\sigma/\sqrt{n_i}$ where σ is the spatial resolution and n_i is the number of events inside the position bin. The weighted r.m.s of mean residuals is $R = \sqrt{\sum_i (r_i/\delta r_i)^2 / \sum_i 1/\delta r_i^2} = \sqrt{\sum_i n_i r_i^2 / \sum_i n_i}$. This is $(17.3 \pm 0.3) \mu\text{m}$ for UTS-5, $(18.0 \pm 0.3) \mu\text{m}$ for CD91 and $(6.46 \pm 0.05) \mu\text{m}$ for the silicon sensor. The weighed distribution of the average residuals is shown in Fig. 3.

In absence of systematic effects on the spatial response of the detector one expects the r.m.s. of mean residuals R to be $R_{\text{stat}} = \sigma/\sqrt{N}$ where N is the average number of entries for each position bin. For silicon it is $R_{\text{stat}} = (6.27 \pm 0.04) \mu\text{m}$ which is indeed close to the measured value. For diamond an important systematic contribution exists, since the measured values of R are much larger than the values expected from statistic fluctuations, $R_{\text{stat}} = (11.65 \pm 0.18) \mu\text{m}$ for UTS5 and $R_{\text{stat}} = (6.53 \pm 0.08) \mu\text{m}$ for CD91.

To quantify the apparent clustering of residual shifts, the linear correlation coefficient between the residuals of all track pairs has been determined. Since each event which passes selection cuts has only one reconstructed track, the pairs are formed considering the tracks of two different events. Correlation coefficients are determined in bins of the distance between the two tracks of a pair. An empirical fit function

$$A \exp(-x/x_0) + a \sin(x/50\mu\text{m} + b)/\sqrt{x} \quad (1)$$

has been found to describe the data of the correlation coefficient of residuals as a function of track separation x . The function is the sum of two components. A sinusoidal modulation with the periodicity of the pixel pitch describes the correlation due to the pattern structure of the sensor. A falling exponential accounts for the residual shifts introduced by the grain structure. The denominator in the exponent x_0 we term the correlation length. It is a measure of the scale of the cluster structure of similar residual shifts.

residual structures.

The residuals correlation is reported in Fig. 4. For silicon the correlation is well described by the pitch modulation term only and the amplitude of the exponential term is consistent with zero.

For diamond the exponential peak is evident. The fit gives a correlation length $x_0 = (36.0 \pm 0.5)\mu\text{m}$ for UTS5 and $(44.4 \pm 0.8)\mu\text{m}$ for CD91. The correlation amplitude A is 0.826 ± 0.016 for UTS5 and 0.748 ± 0.018 for CD91.

The presence of the exponential peak in the diamond correlation distribution is evidence of non-homogeneous charge collection properties producing local systematic shifts in the position response. The investigation of their origin is the subject of the studies described in the next chapter.

4 Simulation of the diamond sensors

In order to understand the experimental results in terms of the microscopic properties of charge carriers drift in diamond, a numerical simulation of the response of diamond sensors to ionizing radiation has been developed.

4.1 The model

The interactions of high-energy pions with the diamond sensor have been simulated using the GEANT4 package [17]. This step of the simulation produces a file with a list of the energy deposits of the particles inside diamond (hits). The energy of each hit is converted into a number of electron-hole pairs using the conversion factor of one pair for 13.1 eV of deposited energy. The charge carriers are then drifted in the diamond in steps of $l = 5 \mu\text{m}$ until they are trapped or they are collected at the electrodes.

Drift model: The drift direction is determined by the local electric field and thermal diffusion. The local electric field is the superposition of the external field of 1040 V/mm and the polarization field created by the charge carriers trapped in the sensor. The diffusion function is a Gaussian with $\sigma = \sqrt{2Dt}$, where D is the diffusivity and t the drift time. The diffusivity D is related to the low-field mobility μ_0 and the temperature T by the Einstein relation $D = \mu_0 kT/e$, where k is the Boltzmann constant and e the elementary charge.

The drift time corresponding to one drift step is $t = l/v$ where the drift velocity v depends on the electric field. It is proportional to the electric field for low field intensity, and reaches saturation in the high-field limit. The following

parametrization was used to connect the two asymptotic behaviors [18]

$$v(E) = \frac{\mu_0 E}{\left[1 + \left(\frac{\mu_0 E}{v_s}\right)\right]} \quad (2)$$

where μ_0 is the low-field drift mobility and v_s is the high-field saturation velocity. The values of these parameters in diamond are controversial [19]. The following values have been used [20,21]: $\mu_0 = 2400 \text{ V}^{-1}\text{cm}^2\text{s}^{-1}$, $v_s = 1.5 \cdot 10^7 \text{ cm/s}$ for electrons and $\mu_0 = 2100 \text{ V}^{-1}\text{cm}^2\text{s}^{-1}$, $v_s = 1.05 \cdot 10^7 \text{ cm/s}$ for holes.

Diamond grains generator: The trapping model presented below requires the simulation of the grain structure of CVD diamond. The grains growth generator is a generalization to three dimensions of the generator described in [7]. The space is divided in small cubic cells ($5 \times 5 \times 5 \mu\text{m}^3$) and the grains are initially 2×2 cells wide. Every time that a layer of cells is added to the diamond film, each cell near the grain border has a probability p to be claimed by a neighboring grain. The resulting conflicts between grains claiming the same space element are solved assigning to each grain a probability to defeat the other proportional to the grain width. This results in large grains getting larger and small grains getting smaller and finally being overgrown. The resulting simulated structure is shown in Fig. 5.

The only parameters of the model are the growth probability p and the film thickness, which is the sensor thickness plus the material removed from the substrate side. The film thickness ($732 \mu\text{m}$) is equal to the final sensor thickness plus the thickness of material removed from the substrate side. The growth probability is chosen so that the resulting spatial residuals correlation length (see Sec. 4.2) agrees with the data.

Trapping model: The probability for a charge carrier to be trapped within the drift step l is $1 - \exp(-l/v\tau)$ where v is the velocity and τ the lifetime.

The lifetime is inversely proportional to the local density of active traps. Different initial trap density distributions have been implemented. In the simulation presented in this paper, the initial trap density depends on the shortest distance to the next grain boundary and is described by [7]

$$n = n_0/[1 - \exp(-r/r_0)] \quad (3)$$

with r the distance to the next grain boundary, n_0 the minimum trap density (deep in the grains bulk) and r_0 the *lifetime length*. The trap density becomes very high near the grain boundaries. This model is supported by observations that the impurity concentration is strongly enhanced at grain boundaries [22,23] thus resulting in a larger density of electrically active traps [7,24].

Priming is simulated by implementing two classes of traps [7]. After they capture a charge, the traps of one class can act as recombination centers, while the traps of the other class are permanently passivated. The electron and hole lifetimes are computed as

$$\tau_e = 1/\beta_e(n_0 + n_+) \quad (4)$$

$$\tau_h = 1/\beta_h(n_0 + n_-) \quad (5)$$

n_0 is the density of unfilled traps of both classes, $n_+(n_-)$ is the density of recombination centers filled with holes (electrons). β can be interpreted as the product of the charge carriers thermal velocity and an effective trapping cross section. It is the same for traps of the two classes but different values can be set for electrons and holes.

When a charged carrier is trapped, the local density of filled and unfilled traps and the local trapped charge density are updated. The polarization field created by the trapped charges is periodically updated and superimposed to the external field to get the electric field map.

As the diamond sensor is exposed to ionizing radiation, three dose-dependent effects occur:

- The pure trapping centers are passivated, so that the effective trap density is reduced, simulating the priming effect.
- Near the electrodes the charge carrier which is drifting toward the electrode is dominant (electrons near the pixels electrodes, holes on the other side). Thus a net space charge density develops. The resulting polarization screens the external field.
- A net space charge develops also near the grain boundaries (only in the scenario with non-uniform trap density). Because of grain lateral growth the boundary surface makes in general a non-zero angle with the z direction. Electrons and holes approach this surface from opposite directions, and are trapped before reaching the interface because of the very high trapping density. Hence a space charge distribution is created, with opposite signs on the two sides of the interface. The electric field they produce is normal to the interface, and has a component which is transverse to the external field. This is the source of the charge drift parallel to the sensor surface.

The distribution of trapped charge for a two-dimensional simulation is shown in Fig. 6. A net negative trapped charge develops near the pixels at the bottom and a net positive charge near the other electrode. The tree-like structures are the boundaries between grains (growing from above). There is a larger trapped charge there, negative above the boundary and positive below it.

The parameters of the trapping model discussed are $n_0, r_0, \beta_e, \beta_h$ and the fraction α of pure trapping centers as explained above. A constraint on the above parameters is provided by the measured value of the average collected charge ($3000 e^-$). This still leaves four degrees of freedom in the parameter choice. Since the other parameters are related to unmeasured properties (such as the priming ratio, or the hole/electron lifetime ratio) it is not possible to determine them from the data.

Some educated guesses have been made instead, with the purpose of building a model which can qualitatively reproduce the features observed in the data, in particular the systematic position shifts. The choice of final values for the parameters is reported below.

- The ratio between hole and electron trapping β_h/β_e was chosen to be 1.5 since measurements with α particles show that holes have a lower lifetime than electrons in diamond sensors [25].
- The fraction α of traps which are permanently passivated upon capture of a charge carrier affects primarily the priming ratio (the ratio between the signals observed in the primed and unprimed state). The value $\alpha = 0.85$ was used. The resulting priming ratio is 1.6 (it is also affected by n_0 , discussed below). The priming ratio of the sensor studied at the test beam is not known, but the simulated value is typical for sensors with good charge collection efficiency [23]. The simulated priming curve is shown in Fig. 7.
- The extent of the region near the crystallite boundaries where trapping is enhanced is determined by r_0 . The value $r = 25 \mu\text{m}$ was chosen. This is smaller than the crystallite size so that in the crystallite bulk the charge lifetime is indeed larger than near the border. A lower value does not change qualitatively the results presented in the next section, but would make them more sensitive to the cell length l of the grid of points on which the trap densities are computed.
- The total trap concentration n_0 at the center of crystallites. The value $n_0 = 2.5 \mu\text{m}^{-3}$ has been used. A smaller value results in a weaker polarization field and thus in a smaller lateral component of the charge drift, in contrast with the experimental evidence. A larger trap density results in too effective external field screening, making it difficult to reproduce a typical priming curve (the signal reaches a maximum then decreases with dose).

The sensitivity of the results of the simulation on each parameter has been computed varying one parameter at a time and retuning β (keeping constant β_e/β_h) so that the mean signal was always equal the experimental value. The resulting variations of efficiency, resolution and systematic shift r.m.s. R are reported in table 2.

Signal formation: At the end of the charge drift algorithm, a list of the positions where the electrons and holes have been trapped or collected is produced.

The charge Q induced on a given pixel electrode is computed as

$$Q = \sum_i q_i [\Phi_w(\vec{r}_i) - \Phi_w(\vec{r}_0)] \quad (6)$$

where q_i are the drifting electric charges, \vec{r}_i is the position at which they were trapped or collected, \vec{r}_0 their initial positions, and Φ_w is the weighting potential [26,27] for the pixel electrode under consideration.

The experimental electronics threshold and noise (1000 e^- and 200 e^- r.m.s.) are simulated.

The pixel hits are processed with the same algorithms used for the analysis of real data. To simulate the telescope extrapolation uncertainty of 6 μm a Gaussian smearing is added to the true track position.

4.2 Results

Due to the severe CPU and memory requirements of a 3D simulation, only a $1 \times 1 \times 0.45 \text{ mm}^3$ volume was simulated. Trap density maps and charge drift were made with a discretization of space in 5 μm steps while the computation of the polarization field was made with a grid with 20 μm pitch.

The diamond samples were in a primed state when data were collected. This was simulated with a sufficiently large number of traversing charged particles to reach a primed state before events for analysis were processed.

The simulated mean spatial residuals as a function of track position are shown in the lower plot of Fig. 8. For comparison, the upper plot reports the results obtained with a uniform trap density (i.e., without simulating the crystallites structure).

The simulation with trapping enhanced near the crystallites boundaries shows systematic shifts as large as 30 μm in the position of the collected charge, as observed with the data (Fig. 2). The agreement with experimental results is much better than using the simulation with uniform trapping⁵.

The same conclusion holds for the residual correlation plot (Fig. 9). In the simulation with uniform trapping (square points) only the readout pitch correlation is observed, and a good fit is obtained omitting the exponential term

⁵ The simulation with uniform trapping has an r.m.s. of mean residuals which is even smaller than the value measured with the data of the silicon sensor. This is due to the fact that the average number of events per bin is larger in the simulation, so statistical fluctuations are smaller.

of eq. 1, as with the experimental silicon data. For the simulation with non-uniform trapping, however, the correlation at small distance scales seen in the diamond data (Fig.4) is reproduced. The simulated residual correlation plot has been fitted with eq. 1.

The correlation length is determined by the average crystallite size, determined by the growth parameter p , and by the trapping parameters, especially the spatial scale for trapping non-uniformities r_0 . The correlation length was tuned to the experimentally measured value by varying p while keeping the trapping parameters constant, except for an overall lifetime scaling to get an average signal equal to the measured value. As p is increased the average crystal size⁶ at the growth surface increases from 0.0119 mm^2 to 0.0422 mm^2 and the correlation length increases from $(21.7 \pm 0.8) \mu\text{m}$ to $(70.4 \pm 1.0) \mu\text{m}$. The final choice of $p = 0.15$, corresponding to an average grain size $A = 0.0238 \text{ mm}^2$, gives a correlation length of $(36.3 \pm 0.4) \mu\text{m}$, in agreement with the observed values.

In table 3 the values of the spatial resolution, the r.m.s. of systematic shifts R (computed as in section 3), the detection efficiency and the residuals correlation length are reported for the two simulations and test-beam data. The statistic error is quoted for simulated values.

The systematic shifts are absent in the simulation without the crystallite structure since they are produced by the lateral component of the polarization field created by charges trapped near the crystallite boundaries. The simulation of the polycrystalline structure is also needed to reproduce the experimental observed detection efficiency of about 70%. When it is omitted the efficiency (respecting the experimental constraints on the average cluster charge and discriminator threshold) is almost 100%. The simulation of the crystallites results in a non-uniform charge collection and regions with reduced detection efficiency. This reproduces the experimentally observed detection efficiency to reasonable accuracy.

While the simulation with enhanced trapping near the grain borders is able to qualitatively reproduce the lateral displacement of charge collection and the residuals correlation at small distance scales observed in the data, these polarization effects are less pronounced in the simulation. As a result, the amplitude and the r.m.s. of systematic shifts R are smaller and the spatial resolution is better in the simulation than in the data.

It is possible to increase the strength of polarization effects with a different choice of the model parameters. In particular, a larger value for n_0 increases the density of traps and thus the polarization charges. However, this also makes

⁶ The average was computed assigning to each crystallite cross section a_j a weight proportional to the probability of a track to cross it. Thus, $A = \Sigma a_j^2 / \Sigma a_j$.

the screening of the external electric field more effective, and it is no longer possible to obtain a priming curve with a flat plateau (Fig. 7), instead the signal reaches a maximum and then decreases, as the field screening prevails over the passivation effect. We have restricted ourselves to choices of the model parameters which give a priming curve typical for diamond sensors exposed to minimum ionizing particles.

Most likely, to achieve a quantitative agreement with the data requires a more accurate trapping model. In the model described in Section 4.1 only two classes of traps have been implemented, pure trapping centres with cross sections σ_e and σ_h for electrons and holes respectively and trapping/recombination centres with the same cross sections σ_e and σ_h both for trapping and recombination processes. In general, several classes of trapping centres should be anticipated, each one with four different cross sections for electron trapping, hole trapping, electron recombination and hole recombination, respectively. In order not to spoil the predictive power of the model by a too large number of free parameters we refrained from introducing these parameters. A detailed microscopic characterization of the number, spatial distribution and trapping cross sections of defect centres in the diamond sensor would be required to better assess the role of these trapping centres and include them in the simulation. That is, however, beyond the scope of the study presented in this paper.

5 Conclusions

Test-beam data were taken with diamond pixel detectors. A detection efficiency of about 70% and a spatial resolution of about 20 μm were obtained. The fine segmentation provided by the pixels and the tracking of the particles by a silicon microstrip telescope allowed a study of the spatial resolution of the detector as a function of the incident position of the particles.

The spatial resolution was found to be degraded by the presence of regions where the reconstructed impact position given by the pixel cluster and the true track position measured with a beam telescope deviate systematically. These regions have the same dimension of the diamond crystallites (about 100 μm) hence they appear to be related to the polycrystalline nature of the sensor.

A model was proposed which attributes the charge collection position shifts to the polarization field created by charges trapped near the crystallite borders, which can have a component parallel to the sensor surface.

A simulation was presented which implements a detailed description of the ionizing particle interactions, the drift and the trapping of charge carriers in

diamond, polarization effects and signal induction on the electrodes. A model for CVD diamond growth was deployed to simulate the crystallite shape in three dimensions, together with a model for the trap density distribution in crystallites.

The simulation is able to reproduce at least qualitatively the lateral displacement of charge collection and the residuals correlation at small distance scales observed in the data, albeit the effect is weaker in the simulation. Detection efficiency for the same amount of collected charge is also reproduced. With a uniform trap density neither the charge collection displacements and residuals correlation nor the detection efficiency can be reproduced.

Acknowledgments

The diamond sensors of the pixel detectors used for the test beam studies were provided by the RD42 collaboration. The front-end electronics chips were provided by the ATLAS Pixel collaboration, which we also acknowledge for use of the test beam setup and beam time. The decoding and reconstruction of test beam data was made with a program developed by A. Andreazza, C. Meroni, F. Ragusa and C. Troncon (INFN and University of Milan).

References

- [1] F. Gianotti et al., hep-ph/0204087 (2002).
- [2] D. Meier et al. (RD42 collaboration), Nucl. Instr. and Meth. A426 (1999) 173.
- [3] W. Adam et al. (RD42 collaboration), Nucl. Instr. and Meth. A447 (2000) 244.
- [4] G. Lindström et al. (RD48 collaboration), Nucl. Instr. and Meth. A466 (2001) 308.
- [5] W. Adam et al., (RD42 collaboration), LHCC-Status-Report-RD-42, CERN-LHCC-2002-010, CERN (2002).
- [6] S. Zhao, Characterization of the electrical properties of polycrystalline diamond films, Ph.D. Thesis, Ohio State University, 1994.
- [7] A. Oh, Particle detection with CVD diamond, Ph.D. Thesis, DESY-THESIS-1999-022.

- [8] M. Ackers et al., IEEE Trans. on Nucl. Sci. 46 (1999) 2033.
- [9] L. Blanquart et al., Nucl. Instr. and Meth. A439 (2000) 403.
- [10] P. Fischer, Nucl. Instr. and Meth. A465 (2001) 153.
- [11] T. Lari, Study of silicon pixel sensors for the ATLAS detector, CERN-THESIS-2001-028 (2001).
- [12] J. Treis et al., Nucl. Instr. and Meth. A490 (2002) 112.
- [13] M. Keil et al., Nucl. Instr. and Meth. A501 (2003) 153.
- [14] L. Blanquart et al., IEEE Trans. on Nucl. Sci. 49 (2002) 1778.
- [15] L. Blanquart et al., FE-I2: A front-end readout chip designed in a commercial 0.25 μm process for the ATLAS Pixel Detector at the LHC, Proceedings of IEEE2003, Oct 2003, Portland, USA.
- [16] I. Gorelov et al., Nucl. Instr. and Meth. A481 (2002) 204.
- [17] The software provided by the GEANT4 collaboration is documented in <http://wwwinfo.cern.ch/asd/geant4/geant4.html>
- [18] C. Jacoboni et al., Solid State Electronics 20 (1977) 77.
- [19] L. S. Pan et al., J. Appl. Phys. 74 (1993) 1086.
- [20] C. Canali et al., Nucl. Instr. and Meth. 160 (1979) 73.
- [21] M. Artuso et al., IEEE Trans. on Nucl. Sci. 26 (1979) 308.
- [22] P. Polesello et al., Phys. Stat. Sol. 154 (1996) 327.
- [23] T. Behnke et al., Diam. and Rel. Mat. 7 (1998) 1553.
- [24] P. Polesello et al., Nucl. Instr. and Meth. A426 (1999) 156.

[25] T. Behnke et al., Nucl. Instr. and Meth. A414 (1998) 340.

[26] S. Ramo, Proc. I.R.E. 27 (1939) 584.

[27] V. Radeka et al., Ann. Rev. Nucl. Part. Sci. 38 (1988) 217.

sensor	UTS-5	CD91	silicon
detection efficiency (%)	76.8 ± 0.5	67.69 ± 0.10	99.61 ± 0.03
mean cluster size	1.484 ± 0.010	1.260 ± 0.001	1.301 ± 0.003
spatial resolution (μm)	23.35 ± 0.21	25.45 ± 0.11	14.46 ± 0.05
R_{meas} (μm)	17.3 ± 0.3	18.0 ± 0.3	6.46 ± 0.05
R_{stat} (μm)	11.65 ± 0.18	6.53 ± 0.08	6.27 ± 0.04
correlation length (μm)	36.0 ± 0.5	44.4 ± 0.8	0
correlation amplitude	0.826 ± 0.016	0.748 ± 0.018	0

Table 1

Summary of the measurements performed on the two diamond detectors. The values for a silicon detector with the same geometry and electronics is presented for comparison.

parameter variation	$\Delta\epsilon(\%)$	$\Delta\sigma$ (μm)	ΔR (μm)
$\beta_h/\beta_e \pm 0.5$	± 0.5	± 0.6	± 0.7
$r \pm 5\mu\text{m}$	± 2	± 0.2	± 0.1
$\alpha \pm 0.05$	± 3	± 0.8	± 1.1
$n_0 \pm 0.5 \mu\text{m}^{-3}$	± 2	± 0.8	± 0.8

Table 2

Sensitivity of the simulation results on parameter choice.

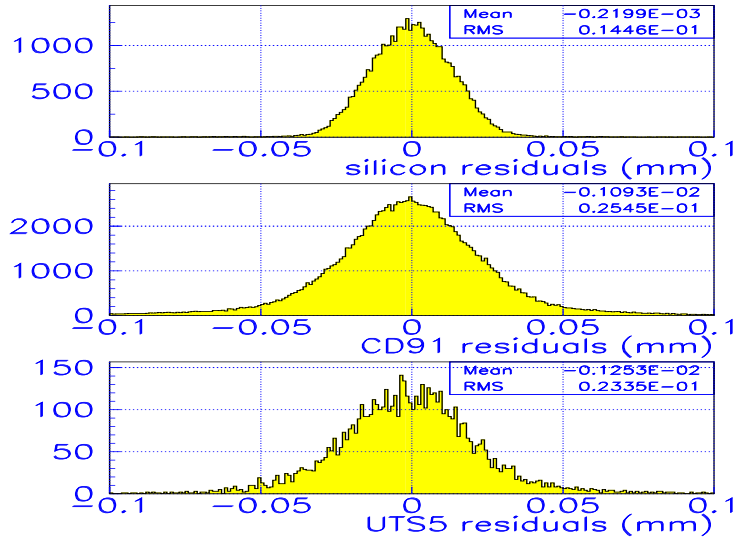


Fig. 1. Residuals between the positions measured by the telescope and by the pixel detector for a silicon detector (top), the CVD-diamond sensor CD91 (center) and UTS-5 (bottom).

sensor	UTS-5	CD91	sim. I	sim. II
spatial resolution (μm)	23.35 ± 0.21	25.45 ± 0.11	19.22 ± 0.06	15.12 ± 0.04
R (μm)	17.3 ± 0.3	18.0 ± 0.3	8.8 ± 0.3	1.08 ± 0.04
detection efficiency (%)	76.8 ± 0.5	67.69 ± 0.10	58.10 ± 0.18	99.54 ± 0.02
correlation length (μm)	36.0 ± 0.5	44.4 ± 0.8	36.2 ± 0.5	0
correlation amplitude	0.826 ± 0.016	0.748 ± 0.018	0.492 ± 0.007	0

Table 3

Spatial resolution, r.m.s. of systematic shifts R (defined in section 3), efficiency, residuals correlation length and amplitude for the data taken with the UTS-5 sensor, the data taken with the CD91 sensor, the simulation with trapping enhanced near the grain borders (I) and the simulation with uniform trapping (II).

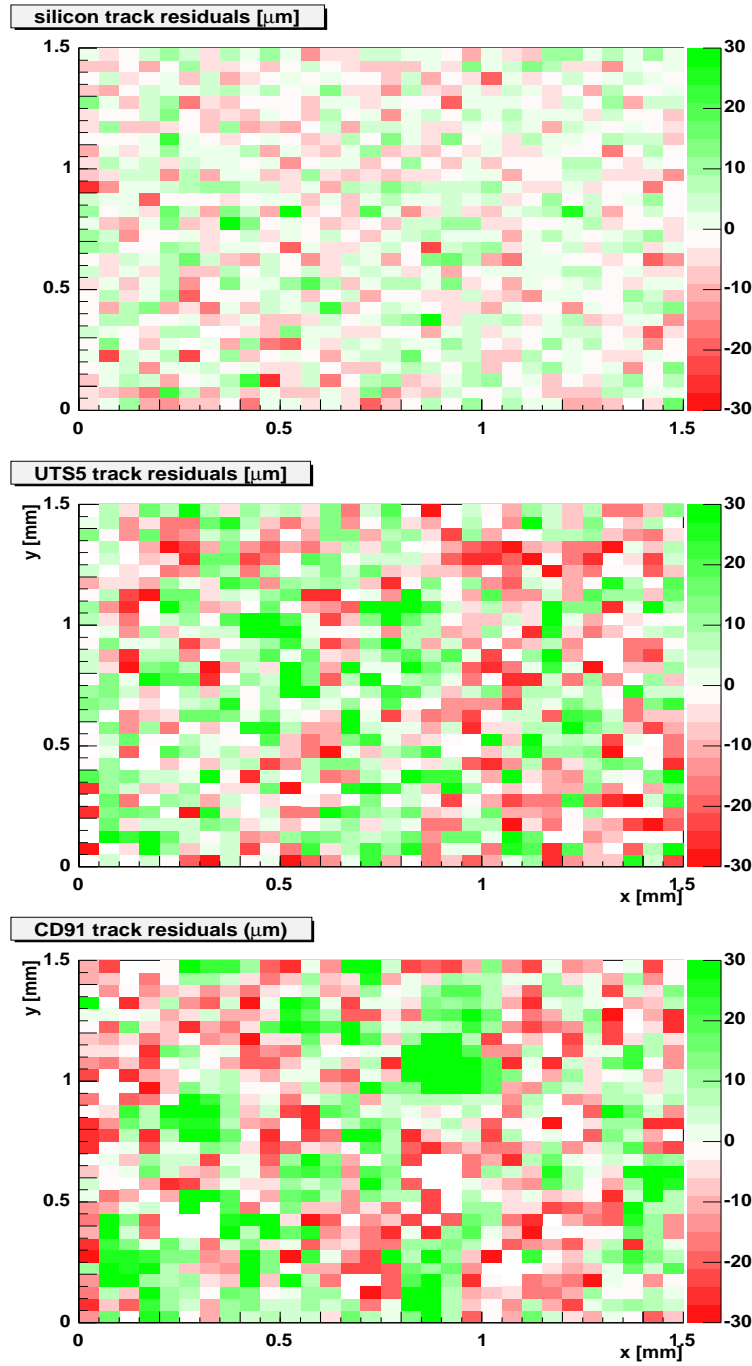


Fig. 2. Mean spatial residual between the position of the center of the pixel clusters and the track position determined by the tracking telescope, as a function of position inside the diamond sensor. The upper plot is for a silicon detector, the middle one for the diamond sensor UTS-5 and the lower plot is for the diamond sensor CD91.

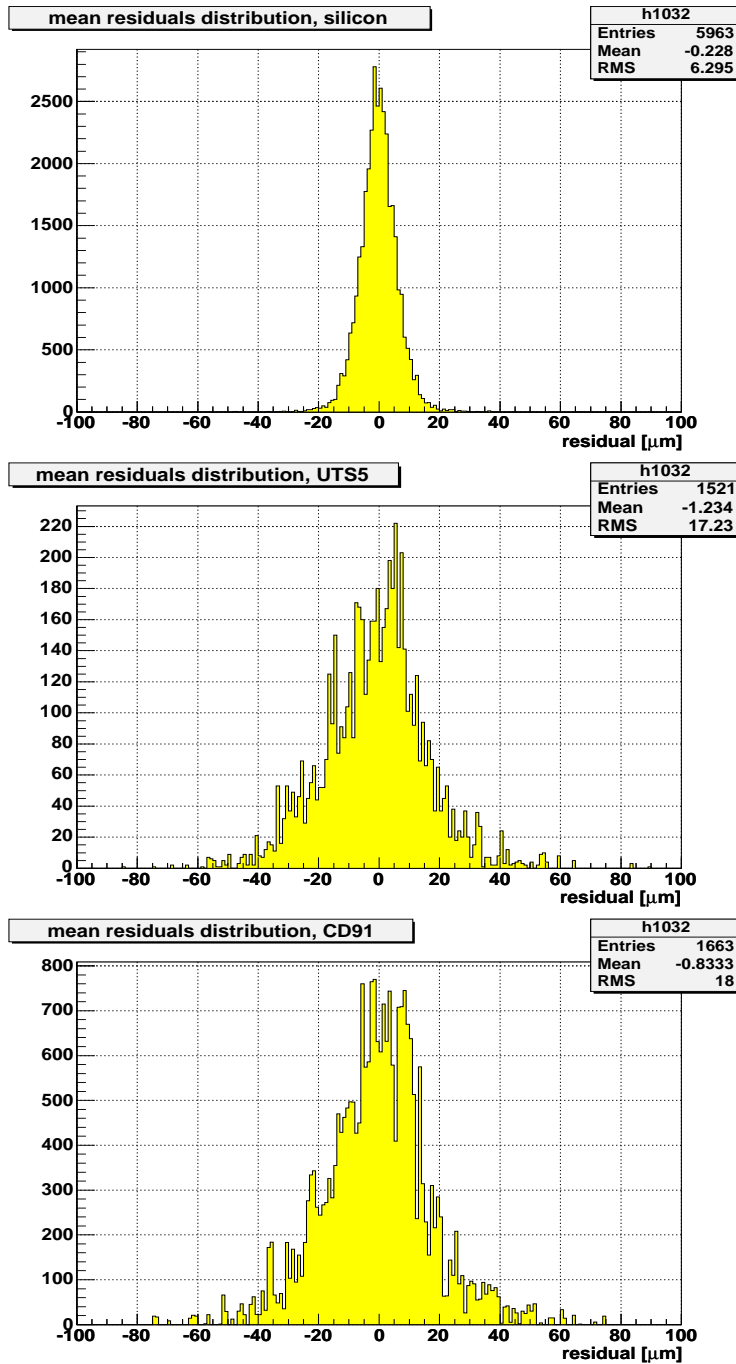


Fig. 3. Distribution of the mean spatial residuals shown in Fig. 2. Each entry (mean spatial residual at a given position) is weighed with the number of tracks used in the computation of the mean residual. The upper plot is for the silicon sensor, the middle one for the diamond sensor UTS-5 and the lower plot is for the diamond sensor CD91.

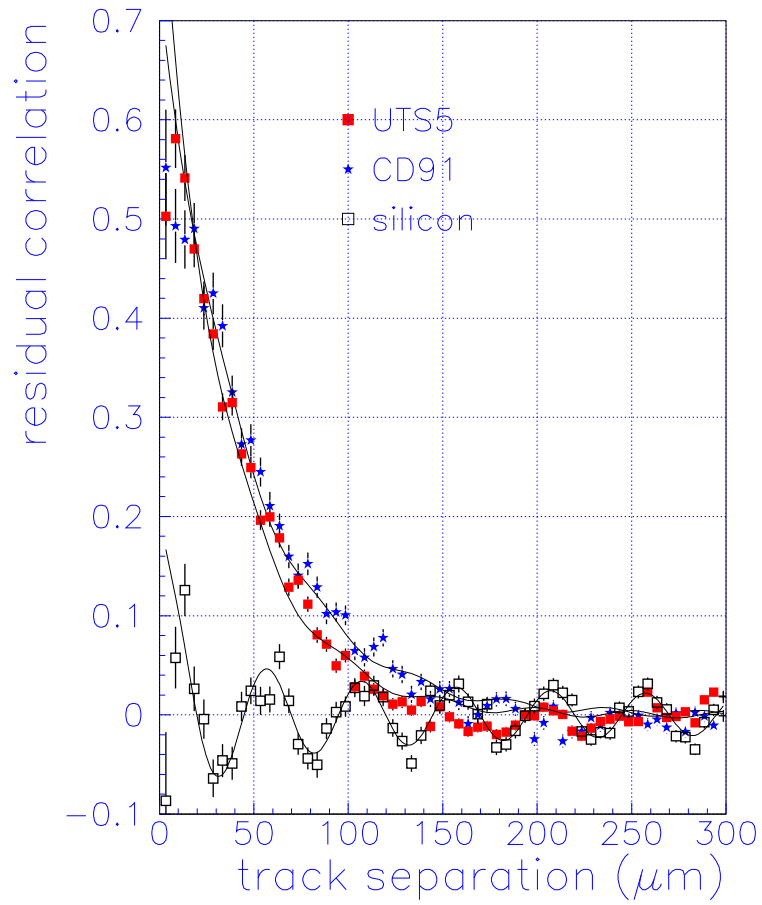


Fig. 4. Correlation between the spatial residuals of two events, as a function of the separation between the tracks of the two events.

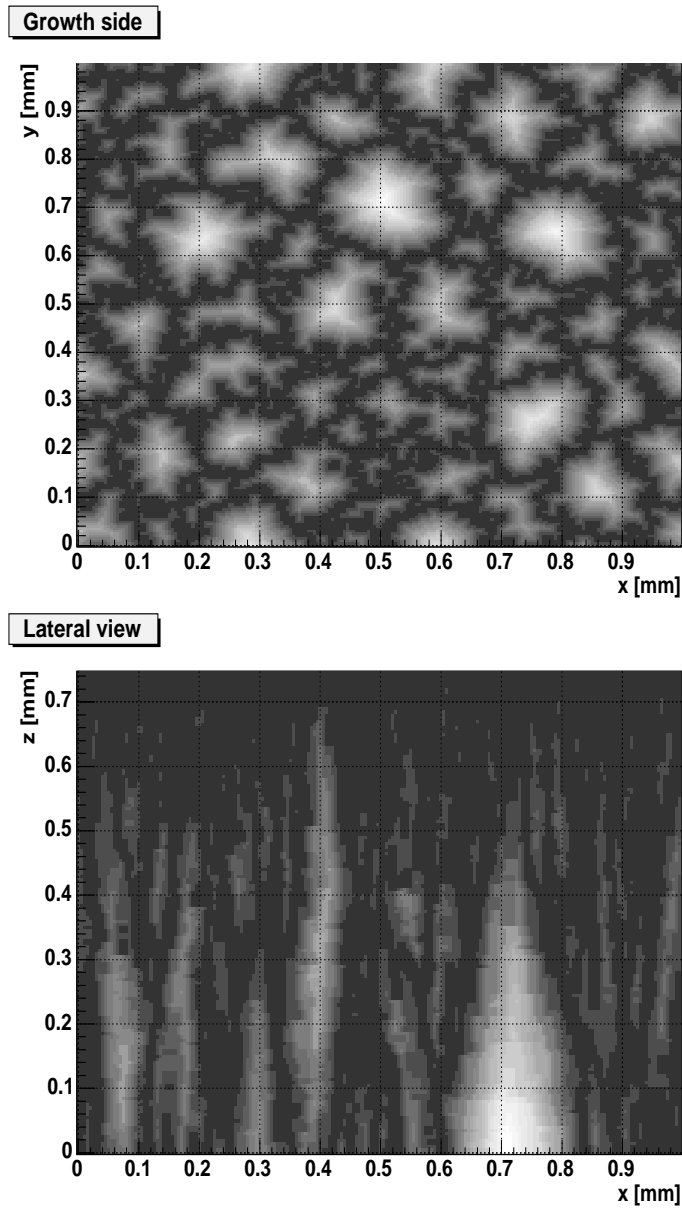


Fig. 5. Three-dimensional simulation of the growth of diamond crystals. The grey scale is proportional to the carrier lifetime, so that the crystallite boundaries are visible as dark region, and the crystallites bulk is white. The upper plot shows the crystallite shapes in a plane perpendicular to the growth direction, on the growth side of the diamond film (where the pixel implantations are made). The lower plot shows the same in a lateral view; the average dimension of crystallites increases from the substrate side of the film (below) to the growth side (above). A thickness of 0.3 mm on the substrate side has been removed after film growth and it is not used in the simulation either.

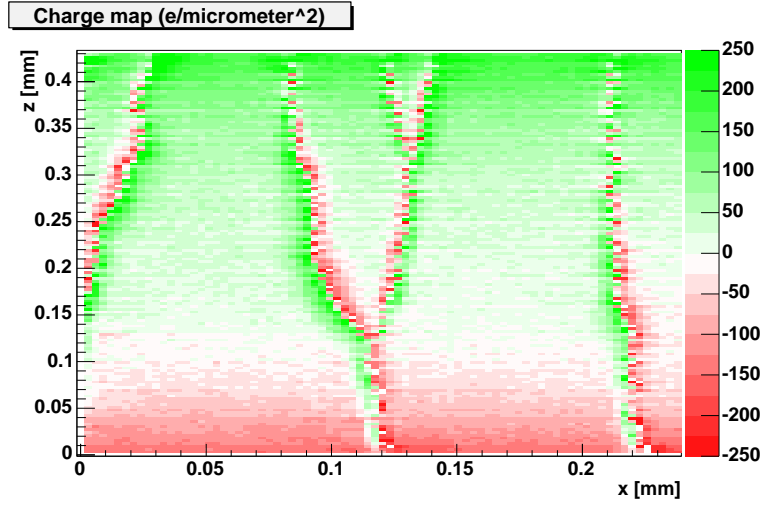


Fig. 6. Trapped charge as a function of position inside the sensor, for a two-dimensional simulation with preferential trapping near the grain boundaries. The crystal growth direction and the external electric field are along the z direction; the pixel implants are located at $z = 0$. The electrons move downward. The grain boundaries are visible as tree-like structures. The pixel electrodes are at the bottom.

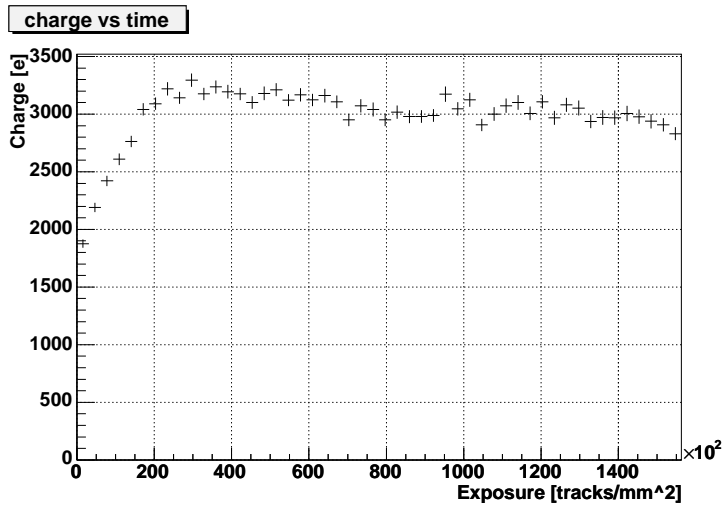


Fig. 7. Priming curve: average charge collected as a function of the exposure resulting from the detector simulation.

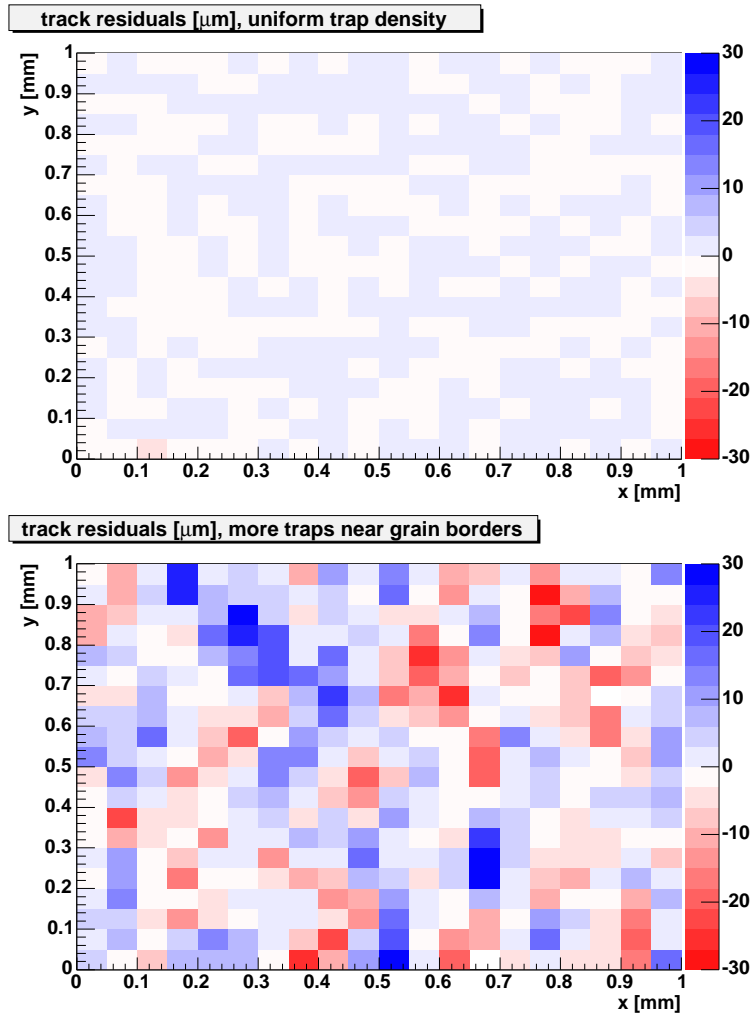


Fig. 8. Mean spatial residual as a function of track position. The upper plot is obtained with the simulation with uniform trap centers density, the lower plot using a higher trap density near the grain boundaries as described in the text.

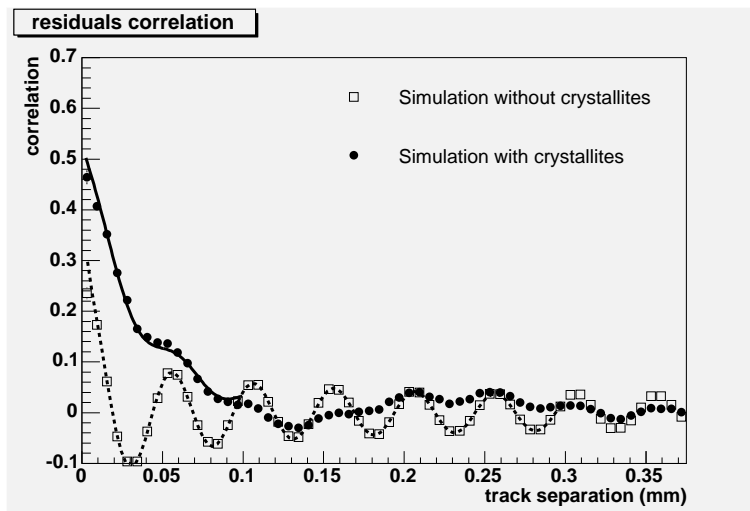


Fig. 9. Track residuals correlation as a function of track position. The squares, fitted with a dashed line, are obtained with the simulation with uniform trap centers density. The circles, fitted with a solid line, are obtained using a higher trap density near the grain boundaries as described in the text.